Manufacturing and characterisation of a composite FishBAC morphing wind tunnel model

Andres E Rivero [1,*], Stephane Fournier[1], Paul M Weaver [1,2], Jonathan E Cooper [3], Benjamin KS Woods [1]

[1]ACCIS, Department of Aerospace Engineering, University of Bristol, Bristol, UK
[2] Bernal Institute in Composite Materials and Structures, University of Limerick, Limerick, Ireland
[3] Department of Aerospace Engineering, University of Bristol, Bristol, UK

Abstract

Compliance-based camber morphing is a promising alternative to conventional aircraft control surfaces, such as rigid trailing edge plain flaps, which vary aerofoil camber in a sharp, sudden and discontinuous way. Unlike traditional trailing edge flaps, camber morphing based on compliant structural design achieves smooth and continuous changes in camber which have been shown to provide a similar lift control authority with significantly reduced drag penalty. One promising camber morphing concept is the Fish Bone Active Camber (FishBAC) device, which is currently being investigated for application to fixed and rotary wing vehicles. In order to extend the understanding of the aerodynamic behavior of this device and also to improve its structural behaviour, a wind tunnel model of a composite FishBAC equipped NACA 23012 wing section has been built. This paper will describe the manufacture of this morphing wing section, and present experimental characterisation of its actuators, the materials and the structural response under actuation loads. Finally, an initial design study is performed to investigate the useful ability of the FishBAC to create spanwise variations in camber, to control spanwise lift distribution and to modify three-dimensional wing stall.

1 INTRODUCTION

Traditional fixed-wing aircraft are controlled by using a series of panels that are hinged to the trailing edge of their wings. These panels are typically trailing edge flaps and, depending on their location and function, they are known as ailerons, elevator, rudder, etc. Although effective in changing the pressure distribution — and hence providing control authority — the change in shape occurs in a sudden and discontinuous manner. These sharp changes in aerofoil shape tend to incur significant drag penalty in operation, as the streamlines separate at the sharp corner that exists when these panels are deflected. This prevents from continuously and actively using these panels during flight, which could be beneficial to actively control aerodynamic forces throughout the entire flight mission.

An alternative to this approach is to still localise the change in shape at the trailing edge, but achieving them in a smooth and continuous way. This is known as variable camber morphing, and it has been widely studied different research groups [1]. Although not a new concept — as there is evidence of variable camber concepts as early as 1920s [2, 3, 4] — there has been considerable interest in recent years in implementing this approach. This is partly due to the need to develop more efficient and quieter aircraft, but also due to developments in smart materials and composite structures. This allows to overcome the main issues that initial variable camber concepts had: heavy and complex mechanisms reduced their benefit.

One approach to achieving smooth camber morphing without excessive mechanical complexity is to design the structure around the concepts of compliance and anisotropy: use material and geometric compliance to create a structure capable of bending along the chord to change camber, but add anisotropic reinforcement (both geometric and material) to maintain stiffness in the other loading directions – thereby isolating the one desired degree of freedom. One of the earlier concepts to implement compliance-based camber change was the DARPA Smart Wing [5], where a central plate, a flexible honeycomb and

*andres.riverobracho@bristol.ac.uk; Phone number: +447955860975

a silicone skin are successfully combined. Others authors, such as De Gaspari et al.[6], developed a compliant 'multi-stiffened' morphing trailing edge device, and manufactured it using 3D printed plastic and a plexiglass skin. The position and shape of their stiffeners is complex, as they result from a stiffness optimisation routine. This would difficult manufacturing this structure using other methods different from additive manufacturing.

Other concepts have focused on proving the use of smart materials and composite structures for either actuating or assisting actuation, such using piezoelectric [7, 8] and shape memory alloy (SMAs) actuators [9, 10] and using bistable composite laminates [11, 12], respectively.

One important, yet not fully exploited element of camber morphing devices, is their potential ability to gradually vary camber along the span. This could be used to control spanwise aerodynamic loads, and further optimise the aerodynamics of the wing. One of the concepts that can achieved is the flexys®flexfoil [13], which can achieve a $\pm 10^{\circ}$ twist along the spanwise direction.

A more recently developed compliance-based camber morphing concept which is showing promising results is the Fish Bone Active Camber (FishBAC) device [14, 15], which is capable of generating large, smooth and continuous changes in camber distribution. Initial wind tunnel testing of a 3D printed plastic version of this concept measured a 20-25% improvement in lift-to-drag ratio compared to a traditional trailing edge flap [16]. These promising results encourage further exploration, and one aspect of the concept which needs further development before it can be implemented is the material choice and construction methods. FishBAC prototypes made to date have use 3D-printed plastic for the structural components (not including the elastomeric skins), which are not really viable materials for commercial aviation. What's more, these materials are essentially isotropic, and so do not provide significant material anisotropy that can be exploited for design purposes, as alluded to above. Carbon fiber reinforced polymer composites, on the other hand, hold much more promise as a material for FishBAC construction due to their excellent material properties, viability for commercial aviation, and their unique ability to be designed and tailored to provide high levels of anisotropic stiffness. It is therefore important to consider composite based FishBAC designs in order to scale-up this technology. Therefore, a composite-spine FishBAC composite wind tunnel model has been designed using a series of analytical aerodynamic and structural tools that are custom-made for this application [17, 18, 19].

The objective of this article is to introduce the design and manufacturing process of the composite FishBAC wind tunnel model, including the characterisation of the materials used and a full study of the actuation mechanism. Furthermore, an initial experimental study of achievable spanwise variations in camber distribution of the FishBAC is presented, which in this work take place on the benchtop under no aerodynamic loading. Finally, the potential aerodynamic benefits of spanwise variations in camber is analysed in two case studies: the first one, by obtaining a spanwise lift coefficient distribution along the span using a low fidelity FishBAC fluid-structure interaction analysis [17], and the second one by visually observing flow separation during stall during a wind tunnel flow visualisation tuft test.

2 WIND TUNNEL MODEL

The Fish Bone Active Camber (FishBAC) device is a camber morphing concept capable of generating large, smooth and continuous changes in camber. It consists of a central load-bearing bending plate (spine) that has a series of spanwise stringers attached, an antagonistic tendon based actuation mechanism and an elastomeric skin. Because the spine is located near the neutral axis, its overall contribution to the aerofoil stiffness is relatively low, allowing for large chordwise changes in camber. Furthermore, the presence of spanwise stringers give the structure an anisotropic nature, making it much stiffer in the spanwise direction than in the chordwise one, helping to isolate the desired degree of freedom.

A composite FishBAC wind tunnel model (Figure 1) is designed and manufacture in order to both validate structural modelling techniques and also to further understand the aerodynamic benefits of variable camber. Being the first FishBAC where fibre-reinforced polymers are used, the design is centered in exploiting the additional level of anisotropy that composite materials provide, which expands the design space and allows for further stiffness tailoring.

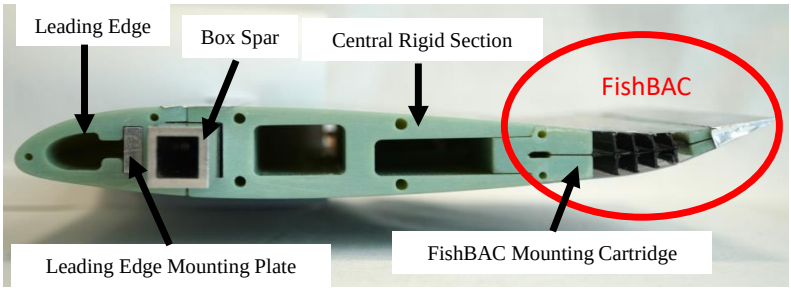

Figure 1. Composite FishBAC wind tunnel model (with upward FishBAC deflection)

2.1 Design

The focus on this first composite FishBAC is the spine, as this is the primary structural member responsible for camber change. For the time being, the other structural components will still by 3D printed, but this work can be considered the first step towards a fully composite FishBAC. Another design objective is to produce a modular wing, where the leading and trailing edge sections can be detached, so that different design configurations can be studied in future work without having to manufacture a full new wing.

For the wing geometry, a NACA 23012 aerofoil with a chord length of $270\,\mathrm{mm}$ with a span of $1\,\mathrm{m}$ is used. This configuration is intended for 2D-wind tunnel testing to further understand the benefits of using the FishBAC device. Furthermore, the FishBAC structural and material sizing and actuator selection are performed using a Kirchoff-Love composite structural model, loaded under representative pressure distributions that are obtained using a one-dimensional fluid-structure interaction routine [18]. Aiming to obtain trailing edge tip deflections of about 10% of the chord length and using the material properties of Hexcel® 8552/IM7 UD prepreg, the FishBAC sizing process lead to the following structural configuration and material selection shown in Table 1. The rigid sections of the wing are designed to resist 150 % of the worst case aerodynamic load at $50\,\mathrm{m\,s^{-1}}$, the maximum rated speed of design.

2.2 Manufacture

The first step of the manufacturing process is to create the carbon fibre spine. The lay-up is performed on a flat aluminium tooling plate, and cured under 8552/IM7's standard autoclave vacuum bag cure cycle — maximum temperature of $180\,^{\circ}\mathrm{C}$ and autoclave pressure of $7\,\mathrm{bar}$. Additionally, three other plates of the same material are cured in the same vacuum bag to allow for measurement of material properties. The plastic parts of the wing are 3D-printed using a Stratasys® Objet^{TM} printer, which uses direct jetting of a liquid photopolymer and cures it under UV light. The composite spine is attached to a plastic mounting "cartridge" (see Figure 1) using a series of transverse screws. In order to fit the screws, holes were drilled into the spine using an end-mill — instead of a drill bit. This is to avoid delamination, as an end-mill uniformly cuts the holes from the edges. Furthermore, the spine is trimmed to size using a diamond saw.

The stringers and the solid trailing edge end of the FishBAC are also 3D-printed on the same Objet printer. The stringers are aligned using a series of laser-cut alignment jigs, and are finally bonded to the carbon fibre plate using Cyanocrylate adhesive.

As mentioned in Section 2, the actuation loads are transferred from the actuators to the FishBAC's trailing edge end using an antagonist tendon configuration. The tendons are made using dry Kevlar-fibre tape coated with Kapton tape, which protects the fibres and keeps them together. The tendons spool around a machined aluminium drive pulley, and are stitched onto the trailing edge of the carbon fibre

Table 1. Preliminary FishBAC and Actuation Sizing

Spine Nominal Thickness	Stacking Sequence	# of stringers	Actuators
$0.375\,\mathrm{mm}$	$[90/0/90]_T$	4	4 × KST X10 HV Servo

spine (through small holes drilled into the spine) with Kevlar tow. After stitching, the tendon is also bonded to the spine using epoxy resin, which provides a combined mechanical and adhesive attachment between tendon and spine.

Finally, a $0.5\,\mathrm{mm}$ 40° thick Shore silicone sheet (Silex Superclear from Silex Silicones LTD) — that acts as the wing skin — is bonded to the FishBAC's mounting cartridge, stringers and solid trailing edge end using a fast cure silicone adhesive (NuSil MED3-4013). Note that, before bonding, the silicone sheet is pre-stretched by 30%. This increases the out-of-plane stiffness of the skin (reducing deformation under aerodynamic loading) and prevents skin buckling.

The remaining solid parts of the wing (i.e. nose leading edge and mid-section) are sanded down by hand and then attached to the main spar using a series of screws. The solid FishBAC's mounting cartridge is fixed to the mid-section of the wing using a series of transverse screws. Finally, paint coating is applied to all plastic parts.

3 MATERIAL CHARACTERISATION

In order to properly model the structural behaviour of the composite FishBAC, a full set of material properties are experimentally obtained for all three types of materials that are used: the ABS-like UV-cured 3D-printed plastic, the carbon fibre prepreg and the silicone skin.

3.1 Hexcel® 8552/IM7 UD carbon fibre prepreg

The material properties of the carbon fibre UD prepreg are obtained in accordance with the ASTM D3039 [20] and ASTM D3518 [21] Standards for obtaining tensile and shear properties of fibre-reinforced polymers, respectively. Two different Instron® tensile machines — $100\,\mathrm{kN}$ and $25\,\mathrm{kN}$ — are used depending on the nature of the specimens. An Imetrum® Video Gauge™ point tracking camera system is used to measure both axial and transverse strains. Three types of tensile tests are peformed: fibre-direction tension, matrix-direction tension and shear. Table 2 shows a summary of the test specimen dimensions, stacking sequence and machine used.

The fibre-direction Young's modulus E_{11} and in-plane Poisson's ratio ν_{12} are obtained from the fibre tension specimens' stress-strain curves (Figure 2), while the matrix-direction Young's modulus E_{22} is obtained from the matrix-direction stress-strain curves. Furthermore, the in-plane shear modulus G_{12} is obtained from the in-plane shear test specimens, and it is calculated from the shears train, obtained by the relationship (Equation 1)

$$\gamma_{12} = \epsilon_x - \epsilon_y \,. \tag{1}$$

It is important to note that all stiffness modulus and Poisson's ratio are obtained by performing a linear fit on the linear portion of each stress-strain curve, and then averaging the linear fit results across all specimens in each set.

3.2 ABS-like 3D printed plastic

The 3D printed plastic was also tested under tension to determine its Young's modulus and Poisson's ratio. A set of dogbone specimens are 3D-printed in accordance with ASTM D638 [22] Standard for

Table 2. CFRP specimen dimensions and stacking sequence. All dimensions correspond to average values across each set of samples

Test	Specimen Thickness	Stacking Sequence	Gauge Length	Width	Machine
Fibre Tension	$1.03\,\mathrm{mm}$	$[(0)_4]_S$	$135.79\,\mathrm{mm}$	$19.80\,\mathrm{mm}$	$100\,\mathrm{kN}$
Matrix Tension	$2.04\,\mathrm{mm}$	$[(90)_8]_S$	$121.35\,\mathrm{mm}$	$25.35\,\mathrm{mm}$	$25\,\mathrm{kN}$
In-Plane Shear	$2.02\,\mathrm{mm}$	$[(\pm45)_4]_S$	$161.00\,\mathrm{mm}$	$25.35\,\mathrm{mm}$	$25\,\mathrm{kN}$

tensile properties of plastic. A Shimadzu® tensile machine fitted with a $10\,\mathrm{kN}$ load cell is used, and strains are measured using an Imetrum video gauge camera system. Average results are summarised in Table 3.

3.3 Silicone Skin

Finally, the Silex® 40° Shore, $0.5\,\mathrm{mm}$-thick skin is tested under tension. The main objective of this test is not only to obtain the Young's modulus and Poisson's ratio, but also to test the strength of the fast cure silicone adhesive. Plastic ABS bonding tabs $50\,\mathrm{mm} \times 25\,\mathrm{mm}$ in planform are 3D-printed and the specimens are created by cutting $200\,\mathrm{mm} \times 25\,\mathrm{mm}$ silicone coupons and then bonding the plastic tabs onto each end with single lap joints. Three of the six specimens had their tabs treated with a chemical primer (Momentive SS4004P) before bonding to determine whether this increases the adhesive shear strength. Based on failure mode, results show that the primer contributed for a material failure (i.e. silicone breaking under tension), rather than adhesive failure. However, even without the primer, failure occurs at much higher strains than those the FishBAC sees during operation. Therefore, it is decided to not use primer to simplify the skin bonding process. One important aspect to point out is that the stress-strain curves (Figure 2) observe a significant amount of non-linearity, as would be expected for an elastomer such as this. Consequently, the Poisson's ratio (as calculated from the results shown in Figure 3) varies depending on the strain.

3.4 Summary of Material Properties

A summary of all the experimentally measured material properties needed to model the structural behaviour of this FishBAC can be found in Table 3:

Table 3. Summary of material properties of the composite FishBAC wind tunnel model. ν_{23} is obtained from a common assumption for CRFP UD laminates, while $G_{23} = E_{22}/2(1+\nu_{23})$

Material	E_{11}	E_{22}	G_{12}	G_{13}	G_{23}	ν_{12}	ν_{13}	ν_{23}
8552/IM7	169.50 GPa	8.58 GPa	5.03 GPa	5.03 GPa	2.96 GPa	0.28	0.28	0.45
ABS Plastic	2.01 GPa		0.73 GPa			0.38		
Silicone Sheet	1.219 MPa		0.44 MPa			0.39		

4 Actuation Characterisation

A total of four KST X10 High Voltage servo actuators are used to drive the tendon spooling pulleys in this FishBAC. They are arranged in mirrored pairs to drive two tendons – one near each end of the wing. Rated for a maximum torque of $1.059\,\mathrm{N\,m}$ (each) at a maximum voltage of $8.4\,\mathrm{V}$, these actuators are capable of producing enough torque to drive the FishBAC, while still fitting inside the NACA 23012 aerofoil profile. Due to limited data provided by manufacturer, a series of studies are performed to fully

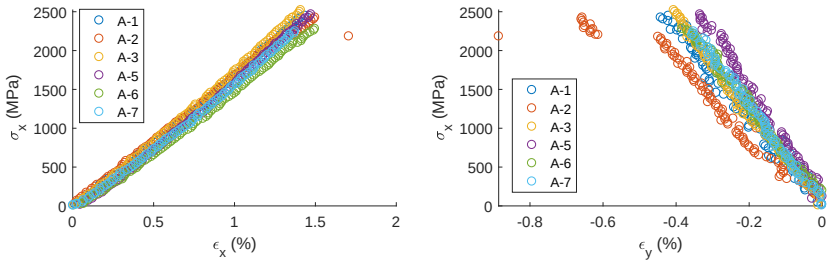

Figure 2. Stress-strain curves of the fibre-direction tensile CFRP specimens

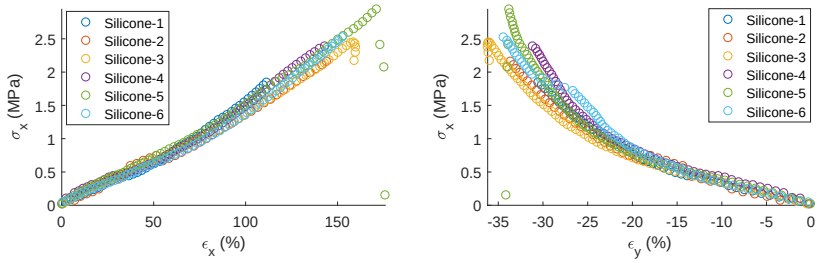

Figure 3. Stress-strain curves of the 40° Shore silicone skin. Specimens 1-3 are bonded to plastic tabs after applying primer, while specimens 4-6 are bonded in absence of primer.

characterise it. First, an angle calibration test is performed using an Arduino servo control routine to calibrate the input vs. output rotation angle. Furthermore, the torque available and torque-power relationship are studied, followed by a thermocouple study to assess the thermal properties of the actuators. Finally, since the Kevlar tendons are hand-stitched to the composite spine, the tendon-pulley system presents some slack due to tension loss during the stitching process. This creates an initial angular range of spooling pulley rotation that does not create camber change, which we define here as the tendon deadband. This was experimentally measured for each tendon.

4.1 Torque-Power Relationship

Following the angle calibration test, a prescribed rotation torsion test is performed to study the relationship between torque available, voltage and power. A Tecquipment® SM1001 30 N m torsion testing machine is used to both prescribe the rotation angle and to measure the corresponding torque for a given actuator operating condition. Using two clamping plates, the servo actuator is clamped to a torque reaction cell in one end, while the other end is connected to a rotating output head through the actuators control horn. The rotating head consists of a hand wheel driving a rotating shaft through a worm gear box, and has an angle sensor to track rotation of the output shaft. Prescribed rotations are applied to the actuator by rotating the turning handle, and the corresponding torque generated by the actuator is measured as a reaction torque (Figure 4).

Once the actuator is fixed to the torque cell, the actuator control input is set to 0° rotation, and the rotating head is slowly turned while angle, torque, actuator voltage and actuator current drawn are recorded. Actuator power draw is the calculated from the voltage and current readings. This test therefore allows for quantification of the relationship between power drawn and torque output for a range of different driving voltages, as shown in Figure 5). Note that the maximum torque available eventually saturates, after which increasing power does not increase torque generated. It can also be observed that, as driving voltage increases, the amount of torque at a given power value decreases. However, increasing voltage increases the maximum torque available.

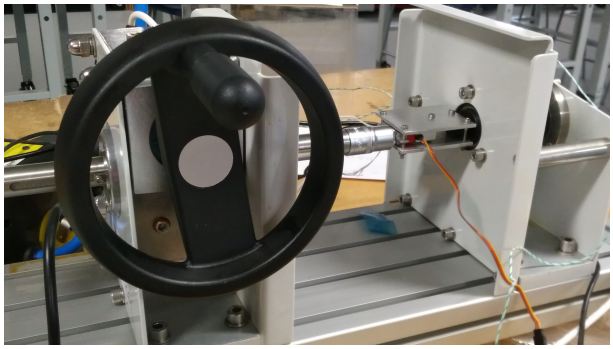

Figure 4. Torsion test rig for actuator characterisation

4.2 Heating

One important aspect of electrical servo motors is self-heating under load, which can lead to damage if not properly monitored and controlled. Actuator temperature response over time and under load is therefore of interest in this study. According to the actuator's data sheet [23], the manufacturer's stated maximum operating temperature of the KST X10 actuators is $65\,^{\circ}\mathrm{C}$. Therefore, a set of thermocouples are used to monitor the increase in temperature, in function of time and voltage. A Pico® TC-08 Thermocouple Data Logger is used to record the temperature of all four actuators when installed inside the wing. The thermocouples are attached to the metal frame of each actuator and they are actuated to their maximum rotation angle and held at that position for several minutes. Also, two more temperature measurements are recorded: one on an actuator wire and one on the plastic surface of the wing. Results show a faster heating rate with increasing voltage, reaching temperatures as high as $80\,^{\circ}\mathrm{C}$ at a voltage of $8\,\mathrm{V}$ (Figure 6) . Furthermore, it can be observed that the actuators driving the left hand tendon (i.e. actuators 1 and 2) heat up faster than the ones in the right tendon. The cause of this is not known, but could be due to asymmetries and misalignment in the actuators' mounting. Finally, these results show that, for voltages between $6\,\mathrm{V}$ and $7\,\mathrm{V}$, temperatures above $65\,^{\circ}\mathrm{C}$ are achieved after the actuator runs for 8 to 10 minutes. As a consequence, and considering the results shown in Figure 5, the actuators will be run at a voltage between $6.5\,\mathrm{V}$ and $7\,\mathrm{V}$. Even though the maximum temperature is exceeded at these voltages, it is important to consider that this test represents an extreme case: maximum actuator rotation angle with no wind speed. During the wind tunnel test, not all runs will be performed at this deflection, and the airflow will dissipate some heat. Nevertheless, the temperature will be monitored, at one of the actuators, during the wind tunnel test.

One particular thermal/electrical property that needs to be investigated is whether torque degrades as temperature increases. To measure this, a thermocouple is added to the torque test setup described in Section 4.1. A prescribed rotation angle of $30°$ and voltage of $6.5\,\mathrm{V}$ is set, and torque and temperature readings and recorded every $10\,\mathrm{s}$. Results show that torque does decrease as temperature increases, showing a reduction of 15% in $10\,\mathrm{min}$ (Figure 7), with the shape of the output torque closely following the temperature curve, and approaching an asymptote. Consequently, it is decided that the actuator temperature needs to be monitored during the wind tunnel test.

4.3 Tendon Rotation Deadband

Since the tendons are hand-stitched to the carbon spine, they may lose tension during the stitching process. As a consequence, the spooling pulley needs to rotate a certain number of degrees in each direction before it starts to apply tension on the tendon. These initial degrees of rotation are defined as the tendon deadband, and will vary between tendons and as a function of rotation direction. To determine these deadbands, a two-camera Imetrum video extensometer system is used to track the tip deflection at both

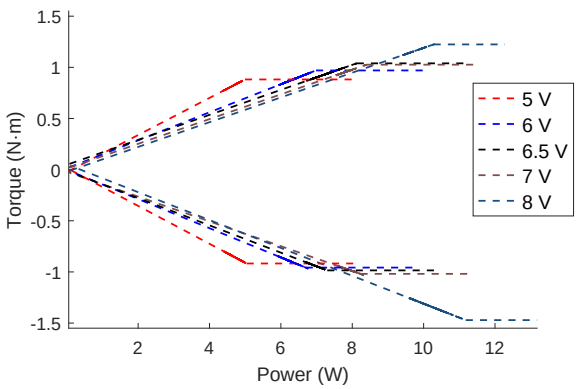

Figure 5. Power vs. torque relationship in function of voltage. Results are obtained by linearly fitting raw data

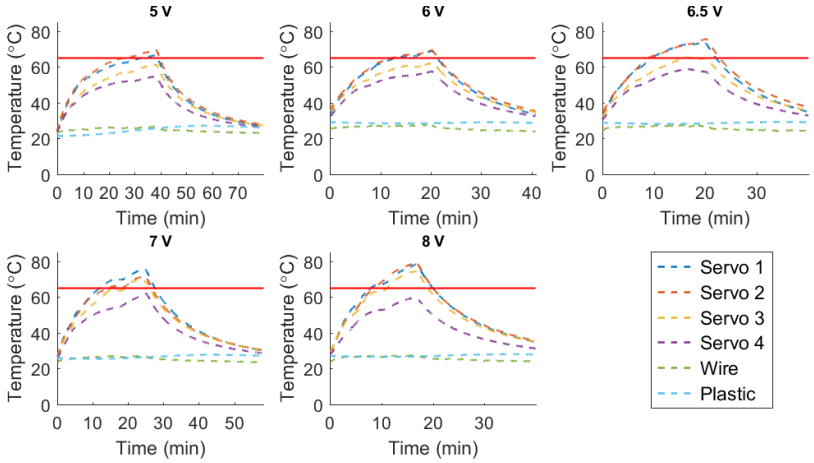

Figure 6. Thermocouple temperature recordings of actuators temperature at maximum actuation angle and in function of voltage

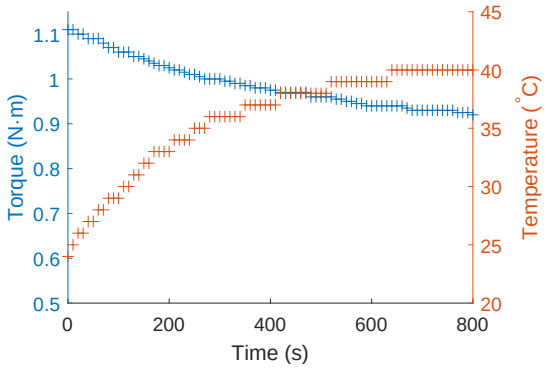

Figure 7. Torque and actuator temperature in function of time. This measurement is performed at a fixed voltage of 6.5 V and actuation angle of 30°

spanwise edges of the FishBAC as a function of actuation angle. Results show (Figure 8) a roughly bilinear response behaviour in both tendons, where the tip deflection slope is very shallow at low angles, and then becomes steeper as the angle increases. This shows that the tendons are able to create some small amount of driving torque even before they are tensioned, but there is also a clear kink in the response upon removal of the slack. The exception to this is the curve for negative rotation angles of the left tendon, which does not show any discernible deadband. These deadbands are compensated for adding angle offsets to the desired values, where the deadband angle for each case is found from the intersection of the two linear fits (dashed lines) in Figure 8.

5 Structural Characterisation: Displacements

A two-camera point tracking Imetrum video gauge system is used to measure the transverse displacement of the FishBAC during actuation —but not under aerodynamic loads— along the trailing edge and on one of the chordwise ends. Voltage and current measurements are recorded from the benchtop power supply. A total of 13 points chordwise and 41 points spanwise are tracked. Three different actuation scenarios are evaluated: uniform loading (i.e. similar tip displacements in both spanwise edges), differential loading with only one actuator applying torque and offset differential loading (different values for each actuator, average input not zero).

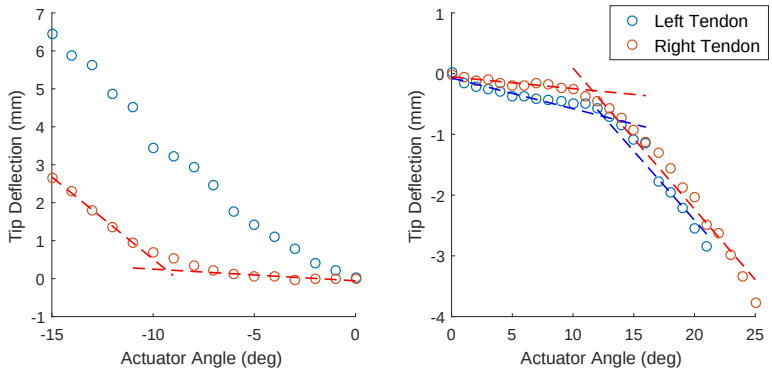

Figure 8. Tip displacement measurements at both spanwise FishBAC ends. Results are used to study the tendon rotation deadband in each tendon-pulley system. Dashed lines are obtained via bi-linear curve fitting

5.1 Uniform Loading

The objective of the uniform loading case is to obtain similar displacements in both spanwise edges. Since there are differences between each actuation-tendon setup — and potentially structural and material imperfections — the pulley angle inputs are adjusted until similar displacements are obtained. Figure 9 shows both chordwise and spanwise deflections under 6 different actuation inputs. The chordwise edge in Figure 9 corresponds to the spanwise location $y = 1000\,\mathrm{mm}$ (right end of the wing). There are a few dropped data points in the spanwise plot due to point tracking issues caused by lighting and reflection, but the overall shapes are well captured. Results show uniform tip deflections at each spanwise end, with a significant variation along the span due to elastic washout. The difference between the deflection at each end (i.e. near the actuation points) and the midspan is between 30% and 43% for all actuation cases. This particular FishBAC was not designed with washout in mind, and the use of plastic stringers does not provide the full degree of obtainable spanwise stiffness (which is the primary driver of elastic washout in this case). Incorporation of higher stiffness materials (e.g. composite) into the stringers would be expected to significantly decrease such washout.

5.2 Offset Differential Loading

The objective of this case is to determine the maximum achievable variation in transverse deflection along the span, when actuation inputs differ in magnitude and direction. The first case to analyse is when only the right end of the FishBAC is actuated, while the other one is kept at zero actuation angle. Figure 10 shows this case, and it can be observed that the transverse displacement can vary as much as $13\,\mathrm{mm}$,

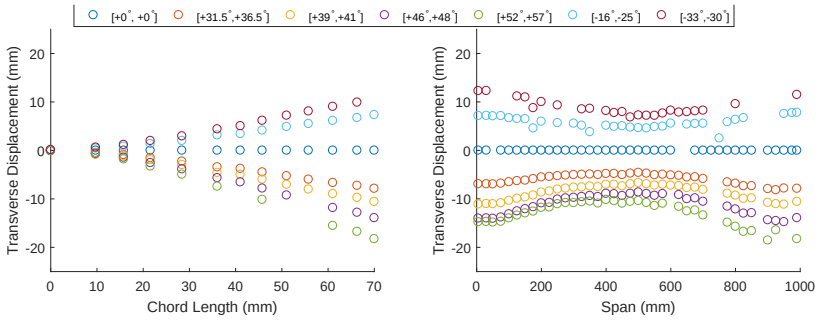

Figure 9. Chordwise (left) and spanwise(right) transverse displacement measurements under symmetric actuation loading. Pulley angles are displayed as [left,right]

which represents a normalised differential displacement of $\Delta(z/c) \approx \pm 4.5\%$ in a $1\,\mathrm{m}$ span.

A second aspect to investigate is whether different shapes can be obtained by applying a constant actuation input on the left-end of the wing — instead of remaining zero. Figure 11 shows three different scenarios where the left-side actuators are given different inputs, while the right-side actuators are kept at a fixed angle. It can be observed that similar tip deflections are achieved, however, the 'average displacement' moves with the different right-side actuation inputs, achieving different spanwise shapes. In each case, spanwise variations — per metre span — of $\Delta(z/c) \approx \pm 4.5\%$, $\Delta(z/c) \approx \pm 5\%$ and $\Delta(z/c) \approx \pm 4\%$ can be achieved, respectively.

6 Spanwise Aerodynamic: Case Studies

The objective of this section is to show examples of how spanwise variations in camber distribution can potentially be exploited for aerodynamic benefit. Two case studies are presented: controlling stall along the span and spanwise lift distribution in terms of lift coefficient.

6.1 Stall Control

One potential benefit of camber variations along the span is the ability to control the spanswise stall locations. In order to prove this, a series of tufts are taped to the composite FishBAC wind tunnel model and the wing is placed inside the Swansea University Subsonic Wind Tunnel. The test is performed at a constant freestream speed of $30\,\mathrm{m\,s^{-1}}$ and the angle of attack is gradually increased until stall is reached at $14°$. Figure 12 shows three cases: an uniform trailing edge down FishBAC deflection (left) and two cases of differential actuation (centre and right). It can be observed that the location where stall occurs varies along the span for all three cases. The stall occurs at the centre of the wing when the FishBAC is actuated uniformly and then shifts towards the side that is actuated to the pressure side (i.e. trailing edge down). This is consistent with the behaviour of traditional trailing edge flaps: stall occurs earlier and at lower angles of attack with increasing downward deflection.

6.2 Change in Lift Coefficient

The FishBAC's ability to vary lift coefficient along the span has not been previously studied. The displacements shown in Figures 9, 10 and 11 can be used to obtain a lift coefficient distribution along the span. To obtain this, an xFoil-based fluid-structure interaction model [17] is used. Lift coefficient is calculated at a fixed freestream velocity of $30\,\mathrm{m\,s^{-1}}$ and angle of attack of $5°$, as it is known that the streamlines reamin well-attached at this angle of attack. It is important to note that there are limitations in this methodology as, although the FSI model does incorporate the strucutral response of the FishBAC, the spanwise displacements used were obtained in absence of aerodynamic loads. Therefore, these spanwise shapes are expected to change — due to increasing spwanwise elastic washout — when freestream

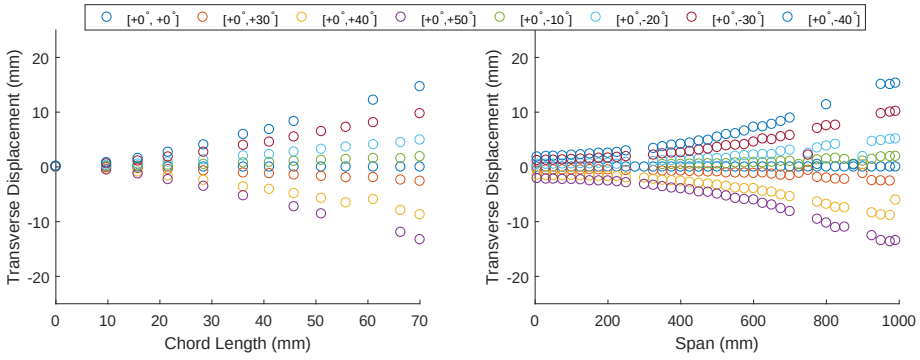

Figure 10. Chordwise (left) and spanwise(right) transverse displacement measurements under actuation of the right hand side of the wing only. Pulley angles are displayed as [left,right]

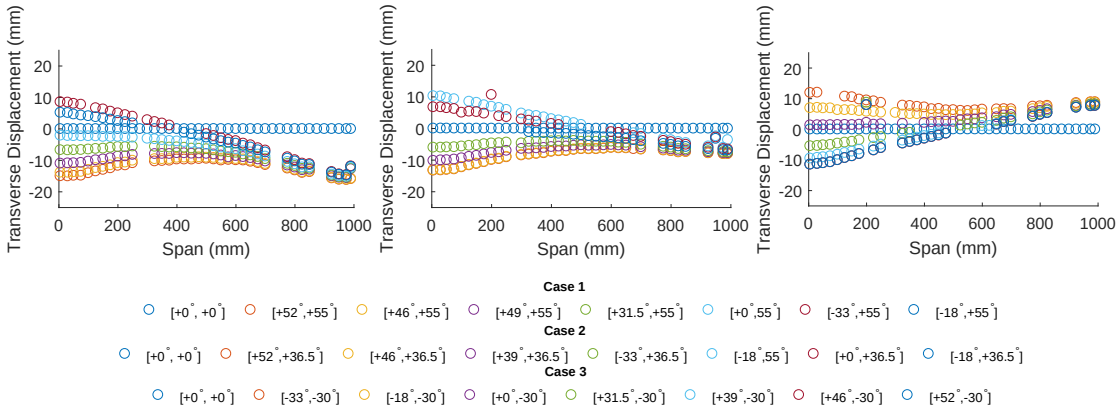

Figure 11. Chordwise (left) and spanwise(right) transverse displacement measurements under offset asymmetric actuation laoding. Pulley angles are displayed as [left,right]

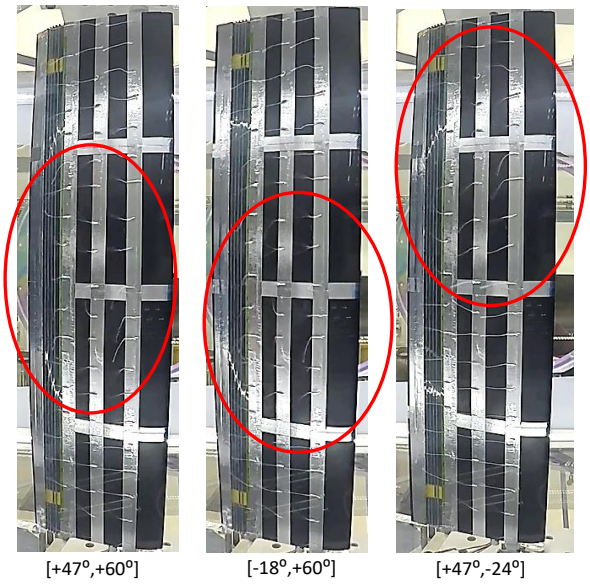

Figure 12. Wind tunnel tuft test to assess FishBAC's ability to control spanwise stall location. Stall regions are enclosed in red ovals

flow is present. Nevertheless, these results can be used as a reference to further understand the FishBAC's ability to control spanwise aerodynamic forces.

Figure 13 presents the spanwise lift distribution of six different actuation cases, selected from Figures 9, 10 and 11, including a zero-actuation case that acts a reference. These selected cases yielded to the most spanwise variation in camber.

Several spanwise lift coefficient shapes are observed in Figure 13, which shows the FishBAC's potential to optimise spanwise aerodynamic behaviour and to reduce induced drag. Also, it can be observed a maximum variation of lift coefficient of 1.09 in a 1 m span (i.e. $\Delta C_L = 1.09$ per metre span). If this quantity is further normalised by the ratio between chord and span, a $\Delta C_{Lnorm} = 0.29$ per unit of span-chord ratio (i.e. $C_{Lnorm} = \Delta C_L \cdot (c/b)$, where c corresponds to the chord length hand b to the span).

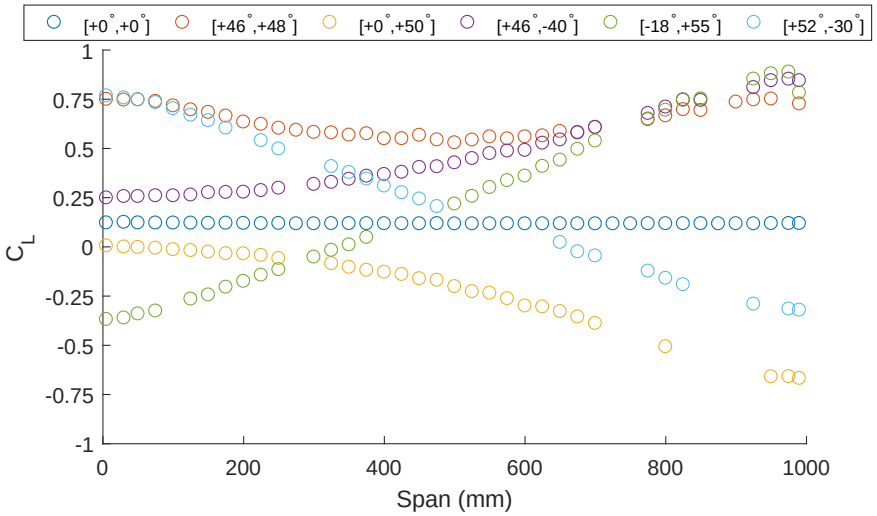

Figure 13. Lift coefficient along the span for several deflection cases. Results are obtained using an xFoil-based FSI routine, at fixed freestream speed of $30\,\mathrm{m\,s^{-1}}$ and angle of attack of $5°$

7 Conclusion

The first composite FishBAC device has been design and manufactured using a combination of materials and manufacturing techniques. A comprehensive structural, material and actuator characterisation has been performed, and the chordwise and spanwise displacements under several actuation load cases have been tracked using a video gauge point tracking system. The novelty of the presented work can be summarised in few key points:

1. A maximum spanwise variation in transverse displacement of $13.5\,\mathrm{mm}$ can be obtained when the FishBAC is loaded asymetrically (i.e. actuation inputs of opposite directions). This corresponds to a variation of $\Delta(z/c) \approx \pm 5\%$.

2. The FishBAC's ability to vary camber distribution along the span could potentially be used to control spanwise stall location — and avoid the whole wing from stalling at the same time.

3. Due to these spanwise variations, an estimated change in lift coefficient of $\Delta C_L \approx 1.05$ per metre span can be obtained. If further normalised, this represents a change in lift coefficient of $\Delta C_L \approx 0.29$ per unit of span-chord ratio.

4. Several spanwise lift coefficients can be obtained, depending on the actuation input combination. These results show the potential ability of the FishBAC to drastically modify the spanwise lift distribution during flight. This could potentially be exploited for induced drag reduction and control purposes.

Acknowledgments

This work was supported by the Engineering and Physical Sciences Research Council through the EPSRC Centre for Doctoral Training in Advanced Composites for Innovation and Science [grant number EP/L016028/1]. Furthermore, this project has received funding from the European Union's Horizon 2020 research and innovation programme under grant agreement No. 723491. The third author would like to acknowledge the Royal Society for the Royal Society Wolfson Merit award and also the Science Foundation Ireland for the award of a Research Professor grant. The fourth author would like to acknowledge the Royal Academy of Engineering for the Research Professorship award.

The first author would like to acknowledge the support provided by Prof. Michael Friswell, Dr Marinos Manolesos and Dr Chen Wang from the College of Engineering at Swansea University (Swansea, UK).

DATA ACCESS STATEMENT

All underlying raw data used in this study are available for download from the Research Data Repository of University of Bristol, data.bris, at: `https://data.bris.ac.uk/data/dataset/2e8tk1wqyjmat2tvyk8fn2fb3h`

REFERENCES

1. Barbarino, S., Bilgen, O., Ajaj, R. M., Friswell, M. I., and Inman, D. J., "A Review of Morphing Aircraft," *Journal of Intelligent Material Systems and Structures*, Vol. 22, No. 9, 2011, pp. 823–877.

2. Parker, H., "The Parker Variable Camber," Tech. Rep. 77, National Advisory Committee for Aeronautics, Washington, DC, 1920.

3. Hogan, H. J., "Variable Camber Airfoil," 1932.

4. Grant, C. H., "Variable Camber Wing," 1939.

5. Kudva, J. N., "Overview of the DARPA Smart Wing Project," *Journal of Intelligent Materials Systems and Structures*, Vol. 15, No. 4, 2004, pp. 261–267.

6. De Gaspari, A., Ricci, S., and Riccobene, L., "Design, Manufacturing and Wind Tunnel Validation of an Active Camber Morphing Wing Based on Compliant Structures," *25th International Conference on Adaptive Structures and Technologies (ICAST 2014)*, , No. January, 2014, pp. 1–12.

7. Bilgen, O., Friswell, M. I., Kochersberger, K. B., and Inman, D. J., "Surface Actuated Variable-Camber and Variable-Twist Morphing Wings Using Piezocomposites," *Structures, Structural Dynamics and Materials Conference*, Vol. 19, No. April, 2011, pp. 1–13.

8. Kota, S., Hetrick, J. A., Osborn, R., Paul, D., Pendleton, E., Flick, P., and Tilmann, C., "Design and application of compliant mechanisms for morphing aircraft structures," *Proc. SPIE*, Vol. 5054, No. November, 2003, pp. 24–33.

9. Sofla, A., Meguid, S., Tan, K., and Yeo, W., "Shape morphing of aircraft wing: Status and challenges," *Materials & Design*, Vol. 31, No. 3, 2010, pp. 1284–1292.

10. Barbarino, S., Pecora, R., Lecce, L., Concilio, A., Ameduri, S., and Calvi, E., "A novel SMA-based concept for airfoil structural morphing," *Journal of Materials Engineering and Performance*, Vol. 18, No. 5-6, 2009, pp. 696–705.

11. Diaconu, C. G., Weaver, P. M., and Mattioni, F., "Concepts for morphing airfoil sections using bistable laminated composite structures," *Thin-Walled Structures*, Vol. 46, No. 6, 2008, pp. 689–701.

12. Daynes, S., Nall, S., Weaver, P., Potter, K., Margaris, P., and Mellor, P., "Bistable Composite Flap for an Airfoil," *Journal of Aircraft*, Vol. 47, No. 1, 2010, pp. 334–338.

13. Flexsys, "flexfoil Variable Gemoetry Control Surfaces," 2014.

14. Woods, B. K. S. and Friswell, M. I., "Preliminary Investigaion of a Fishbone Active Camber Concept," *ASME Conference on Smart Materials, Adaptive Structures and Intelligent Systems*, 2012.

15. Woods, B. K. S. and Friswell, M. I., "Structural Characterization of the Fish Bone Active," *22nd AIAA/ASME/AHS Adaptive Structures Conference, AIAA SciTech*, No. January, 2014.

16. Woods, B. K., Bilgen, O., and Friswell, M. I., "Wind tunnel testing of the fish bone active camber morphing concept," *Journal of Intelligent Material Systems and Structures*, Vol. 25, No. 7, 2014, pp. 772–785.

17. Woods, B. K. S., Dayyani, I., and Friswell, M. I., "Fluid/Structure-Interaction Analysis of the Fish-Bone-Active-Camber Morphing Concept," *Journal of Aircraft*, Vol. 52, No. 1, nov 2014, pp. 307–319.

18. Rivero, A. E., Weaver, P. M., Cooper, J. E., and Woods, B. K., "Progress on the Design , Analysis and Experimental Testing of a Composite Fish Bone Active Camber Morphing Wing," *ICAST 2017: 28th International Conference on Adaptive Structures and Technologies*, Cracow, Poland, 2017, pp. 1–11.

19. Rivero, A. E., Weaver, P. M., Cooper, J. E., and Woods, B. K., "Parametric structural modelling of fish bone active camber morphing aerofoils," *Journal of Intelligent Material Systems and Structures*, 2018, pp. 1045389X1875818.

20. D3039, "Standard Test Method for Tensile Properties of Polymer Matrix Composite Materials," *ASTM International*, Vol. 08, 2014, pp. 1–13.

21. D3518, "Standard Test Method for In-Plane Shear Response of Polymer Matrix Composite Materials by Tensile Test," *ASTM International*, Vol. 94, No. Reapproved, 2007, pp. 1–7.

22. D638, "Standard test method for tensile properties of plastics," *ASTM International*, , No. C, 2013, pp. 1–16.

23. KST, "X10 Wing Servo," *Technical Specifications*, 2017, pp. 2–5.